THE JOURNAL OF BIOLOGICAL CHEMISTRY VOL. 281, NO. 18, pp. 12919–12928, May 5, 2006
Printed in the U.S.A.

Crystal Structure of Prephenate Dehydrogenase from *Aquifex aeolicus*

*INSIGHTS INTO THE CATALYTIC MECHANISM**

Received for publication, November 7, 2005, and in revised form, February 15, 2006 Published, JBC Papers in Press, March 2, 2006, DOI 10.1074/jbc.M511986200

Warren Sun[‡1,2], **Sasha Singh**[‡2,3], **Rongguang Zhang**[§], **Joanne L. Turnbull**[¶], **and Dinesh Christendat**[‡4]

From the [‡]*Department of Botany, University of Toronto, Toronto, Ontario M5S 3B2, Canada, the* [§]*Midwest Center for Structural Genomics and Structural Biology, Argonne National Laboratory, Argonne, Illinois 60440, and the* [¶]*Department of Chemistry and Biochemistry, Concordia University, Montreal, Quebec H4B 1R6, Canada*

The enzyme prephenate dehydrogenase catalyzes the oxidative decarboxylation of prephenate to 4-hydroxyphenylpyruvate for the biosynthesis of tyrosine. Prephenate dehydrogenases exist as either monofunctional or bifunctional enzymes. The bifunctional enzymes are diverse, since the prephenate dehydrogenase domain is associated with other enzymes, such as chorismate mutase and 3-phosphoskimate 1-carboxyvinyltransferase. We report the first crystal structure of a monofunctional prephenate dehydrogenase enzyme from the hyperthermophile *Aquifex aeolicus* in complex with NAD^+. This protein consists of two structural domains, a modified nucleotide-binding domain and a novel helical prephenate binding domain. The active site of prephenate dehydrogenase is formed at the domain interface and is shared between the subunits of the dimer. We infer from the structure that access to the active site is regulated via a gated mechanism, which is modulated by an ionic network involving a conserved arginine, Arg^{250}. In addition, the crystal structure reveals for the first time the positions of a number of key catalytic residues and the identity of other active site residues that may participate in the reaction mechanism; these residues include Ser^{126} and Lys^{246} and the catalytic histidine, His^{147}. Analysis of the structure further reveals that two secondary structure elements, $\beta 3$ and $\beta 7$, are missing in the prephenate dehydrogenase domain of the bifunctional chorismate mutase-prephenate dehydrogenase enzymes. This observation suggests that the two functional domains of chorismate mutase-prephenate dehydrogenase are interdependent and explains why these domains cannot be separated.

The biosynthesis of tyrosine is of critical importance for the growth and survival of enteric bacteria, yeasts, fungi, and plants. Like the other aromatic amino acids, tyrosine plays a dual role in the biochemistry of the organism, acting as both a product and a precursor. In the former case, tyrosine is required for protein synthesis, whereas, in the latter, it is a substrate for enzymes in downstream metabolic pathways. The aromatic metabolites derived from tyrosine include quinones (1, 2), cyanogenic glycosides (3), alkaloids (4, 5), flavonoids (6), and phenolic compounds derived from the phenylpropanoid pathway (6, 7). Since many of these compounds are involved in primary biological processes, they are essential for viability. In plants, for example, flavonoids are important for normal development, since they are involved in auxin transport (8–10), pollen germination (8, 11, 12), and signaling to symbiotic microorganisms (8, 13).

The first committed step in tyrosine biosynthesis involves the conversion of prephenate to either L-arogenate or 4-hydroxyphenylpyruvate. Enzymes in the TyrA family of dehydrogenases, which are dedicated to L-tyrosine biosynthesis (14), are classified into one of three groups, depending on their substrate specificities. Prephenate dehydrogenases (PDHs)[5] accept prephenate, arogenate dehydrogenases utilize arogenate, and cyclohexadienyl dehydrogenases can utilize either compound as substrate. The current paper focuses on the PDH enzyme. This enzyme catalyzes the oxidative decarboxylation of prephenate to 4-hydroxyphenylpyruvate in the presence of NAD^+ (15) (Scheme 1) and is of paramount importance, since it channels prephenate, a branch point intermediate in tyrosine and phenylalanine biosynthesis, to tyrosine synthesis.

PDHs exist as either monofunctional or bifunctional enzymes. The bifunctional enzymes are diverse, since the prephenate dehydrogenase domain is associated with other enzymes (16), such as chorismate mutase and 3-phosphoskimate 1-carboxyvinyltransferase. Biochemical studies on PDH from the bifunctional *Escherichia coli* enzyme, chorismate mutase-prephenate dehydrogenase (CM-PDH), have been conducted in detail (17, 18). Kinetic analyses of wild-type and site-directed variants of the PDH domain, in addition to biophysical studies, have already identified some of the key residues involved in the oxidative decarboxylation reaction (17, 18). Studies of the pH dependence for the kinetic parameters V and V/K, for example, indicated that a deprotonated group is required for catalysis, whereas a protonated residue is required for binding prephenate to the enzyme-NAD^+ complex (18). Moreover, mutagenesis of His^{197} from the PDH domain of CM-PDH revealed that this residue is critical for dehydrogenase activity and that it is one of the groups titrating in the pH rate profile (18). These results suggest that His^{197} facilitates hydride transfer from prephenate to NAD^+ by hydrogen bonding to and polarizing the 4-hydroxyl group of prephenate (18). Additional mutagenesis studies of CM-PDH have also led to the identification of a key binding group, Arg^{294}, which is important for positioning prephenate in the enzyme-NAD^+ complex (17).

* This work was supported by a grant from the Natural Science of Engineering Research Council of Canada. Use of the Argonne National Laboratory Structural Biology Center beamlines at the Advanced Photon Source was supported by the United States Department of Energy, Office of Energy Research, under Contract W-31-109-ENG-38. The costs of publication of this article were defrayed in part by the payment of page charges. This article must therefore be hereby marked "*advertisement*" in accordance with 18 U.S.C. Section 1734 solely to indicate this fact.

The atomic coordinates and structure factors (code 2G5C) have been deposited in the Protein Data Bank, Research Collaboratory for Structural Bioinformatics, Rutgers University, New Brunswick, NJ (http://www.rcsb.org/).

[1] Supported by a University of Toronto Fellowship.

[2] These authors contributed equally to this work.

[3] Supported in part by the Ontario Graduate Scholarship in Science and Technology program and a University of Toronto Fellowship.

[4] To whom correspondence should be addressed: Dept. of Botany, University of Toronto, 25 Willcocks St., Toronto, Ontario M5S 3B2, Canada. Tel.: 416-946-8373; Fax: 416-978-5878; E-mail: dinesh.christendat@utoronto.ca.

[5] The abbreviations used are: PDH, prephenate dehydrogenase; CM, chorismate mutase; PDH-3-PSK, 3-phosphoskimate 1-carboxyvinyltransferases; DALI, distance matrix alignment; FL, full-length; NTA, nitrilotriacetic acid; MALDI-TOF, matrix-assisted laser desorption ionization time-of-flight.

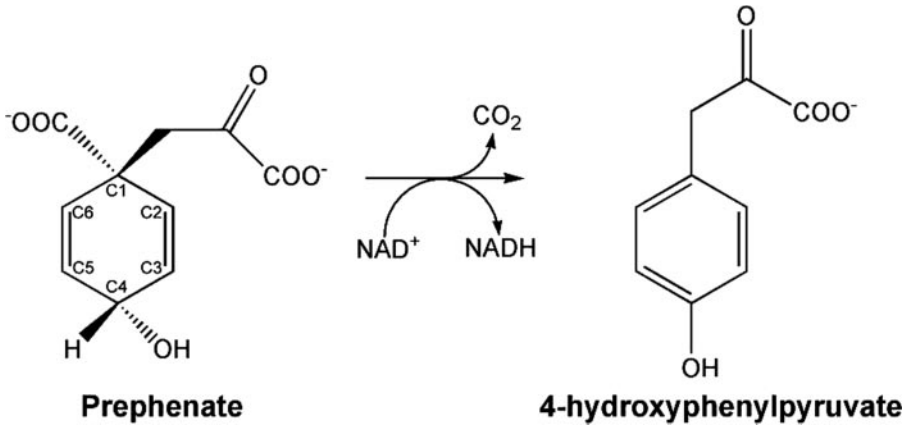

SCHEME 1. **NAD^+-dependent oxidative decarboxylation of prephenate catalyzed by prephenate dehydrogenase.**

Further analyses of the activities of wild-type protein and site-directed mutants in the presence of a series of inhibitory substrate analogues have suggested that this arginine binds prephenate through the ring carboxylate. Although these residues are implicated in the PDH catalytic mechanism, their precise roles in substrate binding and catalysis and their positions in the active site are still tentative. Therefore, a crystal structure of PDH is essential in order to understand the kinetic mechanism of this enzyme.

Here we present the first representative structure of an enzyme in the TyrA family. We have determined the crystal structure of a PDH enzyme from the hyperthermophile *Aquifex aeolicus* in complex with NAD^+ and with prephenate modeled into the active site. Furthermore, the structure of the C-terminal domain from *A. aeolicus* PDH represents a novel fold. The structure reveals a shared active site in the dimer. Interestingly, we infer from the structure that access to the active site is regulated via a gated mechanism, which is modulated by an ionic network involving a conserved arginine. In addition, the crystal structure reveals for the first time the positions of a number of key catalytic residues and the identity of other active site residues that may participate in the reaction mechanism. This PDH structure will provide a basis for understanding the mechanism of substrate discrimination between the different classes of TyrA enzymes.

The rational design of drugs and herbicides will also be facilitated by the structure of PDH. The requirement for tyrosine in protein translation and in the production of biologically important metabolites has made PDH a potential target for the development of novel drugs. The potential of such structure-based research can be gleaned from the success of the broad spectrum herbicide glyphosate, which targets the main trunk of aromatic biosynthesis, the shikimate pathway (19). This herbicide, in addition to its role in weed management, has been shown to be an effective drug for targeting apicomplexan parasites, such as *Plasmodium falciparum* for the treatment of malaria (20).

MATERIALS AND METHODS

Cloning—Gene sequences encoding the various constructs of *A. aeolicus* VF5 PDH (gi:15282445) were amplified by PCR from a pET15b plasmid containing the full-length (FL) PDH gene. The preparation of the FL PDH plasmid is described elsewhere.[6] For all constructs, the forward primers included an NdeI restriction site, whereas the reverse primer contained a BamHI site. Primer sequences for all constructs are summarized in Table 1. The PCR-amplified gene products were subsequently cloned into a pET15b vector (Novagen), which harbors a cleavable N-terminal hexahistidine tag.

[6] J. Turnbull, manuscript in preparation.

TABLE 1
Primer sequences

Construct	Forward primer
Δ19-PDH	GCGGCGGCCCATATGAATATTATAAAAATTTTAAAA TCTTTAAG
Δ25-PDH	GCGGCGGCCCATATGAAATCTTTAAGTATGCAAAAC
Δ28-PDH	GCGGCGGCCCATATGAGTATGCAAAACGTCCTC
Δ36-PDH	GCGGCGGCCCATATGGGCGTGGGCTTTATGG
Δ52-PDH	GCGGCGGCCCATATGGGGTTTAAGGGAAAAATATAC
Δ55-PDH	GCGGCGGCCCATATGGGAAAAATATACGGGTAC
PDH-rev[a]	GCGCGGATCCATCTATCTCCATTCTCTTAATC

[a] The reverse primer was used for each forward primer.

Protein Expression and Purification—All constructs *of A. aeolicus* VF5 PDH were expressed and purified as previously described (21). Briefly, the expression plasmid for PDH was transformed into *E. coli* BL21-Gold (DE3) (Stratagene), which harbors an extra plasmid (pMgk) encoding three rare tRNAs (AGG and AGA for Arg, ATA for Ile). These *E. coli* cells were then cultured in 1 liter of Luria-Bertani medium supplemented with ampicillin (100 μg/ml) and kanamycin (50 μg/ml) and incubated at 37 °C with shaking until the culture reached an A_{600} of 0.6–0.8. At this point, the culture was induced with 0.4 mM isopropyl β-D-thiogalactopyranoside for 3 h at 37 °C with shaking and allowed to grow overnight at 15 °C. Cells were harvested by centrifugation and disrupted by sonication, and the insoluble cellular material was removed by centrifugation. The PDH protein was purified from other contaminating proteins using Ni-NTA affinity chromatography. The protein was digested with 1 μg of thrombin/mg of purified protein for 16 h at 4 °C and then passed through a Ni-NTA column to remove the cleaved histidine tags. The protein was subsequently dialyzed, stored in buffer containing 10 mM HEPES (pH 7.5) and 500 mM NaCl, and quantified using an extinction coefficient of 25,900 M^{-1} cm^{-1}. For the Δ19-PDH construct, selenomethionine protein was prepared as follows. Δ19-PDH was expressed in BL21 cells (described above) in M9 minimal medium (22) containing 0.4% (w/v) glucose as a carbon source. Once the cells reached an A_{600} of 0.8, selenomethionine plus an amino acid mixture (60 mg of selenomethionine; 100 mg of lysine, threonine, and phenylalanine; and 50 mg of leucine, isoleucine, and valine) were added. The culture was induced 15 min later with 0.4 mM β-D-thiogalactopyranoside, and the cells were allowed to grow as described above for the native protein. Cell lysis and protein purification were carried out exactly as described above for native protein but with the addition of 5 mM β-mercaptoethanol in all buffers.

Limited Proteolysis of Full-length PDH, MALDI-TOF Analysis, and Construct Design—The expressed FL PDH protein rapidly degraded, and crystals obtained from this preparation were unstable. As a result, limited proteolysis was conducted on the FL PDH protein solution to

remove protease-susceptible regions and to obtain a stable protein product. Briefly, the PDH protein was incubated with 40 ng of trypsin, 100 μl of 10 mg/ml PDH protein in 100 mM ammonium bicarbonate at pH 8.5 and was analyzed at various time points (Fig. 1). The reaction was stopped by lowering the pH to 5.0 using HCl. The partially digested protein was resolved by 12% SDS-PAGE. The band representing a stable protein product was excised from the gel, and in-gel tryptic digestion was subsequently conducted. The peptides resulting from digestion were extracted and then analyzed on a MALDI-TOF instrument (Bruker Autoflex) to identify N- and C-terminal peptides. Briefly, peptides eluted in 50% acetonitrile and 5% formic acid were mixed with α-cyano-4-hydroxycinnamic acid matrix in a 1:1 ratio in 50% acetonitrile and 0.1% trifluroacetic acid and spotted onto a target plate, and MALDI-TOF mass spectrometry analysis was conducted. The Mascot data base was used to identify peptides that corresponded to the observed masses. Based on this analysis, constructs Δ19-PDH, Δ25-PDH, Δ28-PDH, Δ36-PDH, Δ52-PDH, and Δ55-PDH, which lack the first 19, 25, 28, 36, 52, and 55 residues, respectively, were designed.

Gel Filtration—Gel filtration was performed with a Superdex 200 prep 16/60 column (GE Healthcare) equilibrated in 10 mM HEPES (pH 7.5) and 500 mM NaCl using AKTA Explorer (GE Healthcare). The protein standards used were bovine serum albumin, ovalbumin, and cytochrome *c*. Chromatography was performed at 4 °C at a flow rate of 0.5 ml/min.

Crystallization—The initial crystallization condition was determined with a sparse crystallization matrix (Hampton Research Crystal Screen I^{TM}) at room temperature using the hanging drop vapor diffusion technique. The optimized crystallization condition consists of 12% polyethylene glycol 4000, 100 mM sodium acetate at pH 3.2, and 200 mM lithium sulfate (2 μl of protein solution (15 mg/ml) plus 2 μl of the reservoir solution). Crystals selected for single wavelength anomalous dispersion data collection were flash-frozen in a 12.5% glycerol solution as a cryoprotectant.

X-ray Diffraction and Structure Determination—X-ray diffraction data were collected from a single crystal at a temperature of 100 K in a nitrogen stream on beamline 19ID at the Advanced Photon Source at Argonne National Laboratories (Argonne, IL). The diffraction data were processed and scaled with the HKL2000 suite of programs (DENZO/SCALEPACK) (23). Initial phase information was obtained with SOLVE (24), from which 28 selenium sites were identified using the single wavelength anomalous dispersion phasing method with the selenium peak diffraction data. Phase improvements were achieved by density modification and noncrystallographic symmetry averaging with RESOLVE (25). Initial model building was done using RESOLVE followed by ARP/wARP (26), which built a total of 917 residues for the tetramer (79% of the complete model). The remainder of the model was manually built with O (27), and simulated annealing refinement was subsequently conducted with CNS (Crystallography and NMR System) (28) after every round of model building. A total of six rounds of model building with O and CNS refinement were conducted. All four molecules of PDH were rebuilt prior to every round of refinement, and noncrystallographic restraint was not applied during CNS refinement. The NAD^+ molecules were fitted to the unaccounted electron density in each molecule in the tetramer after the second round of refinement. Subsequently, water molecules were added after the fourth round of refinement. Water molecules were initially picked using CNS and then manually verified in O using the following criteria: a peak of a least 2.5 σ in an $F_O - F_C$ map, a peak of at least 1.0 σ in a $2F_O - F_C$ map, and reasonable intermolecular interactions. NAD^+ and prephenate Protein Data Bank codes, topology, and parameter files were obtained from the HIC-up server (available on the World Wide Web at x-ray.bmc.uu.se/hicup). Figures were produced with MolScript (29), PyMol (W. DeLano; DeLano Scientific, San Carlos, CA), and SPOCK (J. Christopher; Center for Macromolecular Design, Texas A & M University, College Station, TX).

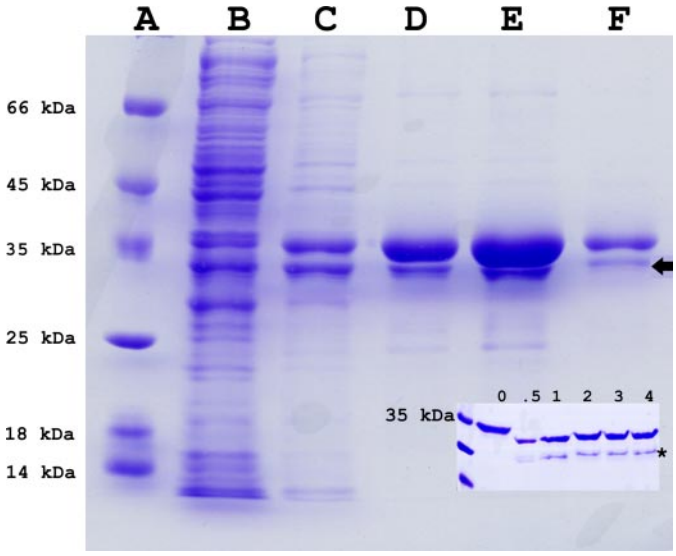

FIGURE 1. **The expression profile and proteolytic susceptibility of the full-length *A. aeolicus* PDH.** SDS-PAGE of collected fractions of the FL PDH purified protein is shown. *Lane A*, molecular weight marker; *lane B*, crude lysate; *lane C*, flow-through; *lanes D–F*, eluted fractions. The expected molecular mass of the FL PDH recombinant is ~36 kDa (predominant band), but a lower molecular weight species (*arrow*) is also present throughout purification. *Inset*, tryptic digest analysis of the FL-PDH protein (without the N-terminal histidine tag) at 0, 0.5, 1, 2, 3, and 4 h of trypsin incubation shows a stable digestion product of ~32 kDa. The band corresponding to trypsin is indicated by an *asterisk*, and the 35-kDa marker is labeled (*inset*).

Multiple Sequence Alignment—Multiple sequence alignment was conducted with T-COFFEE (32). Sequences from six monofunctional PDHs and from the PDH domains of eight bifunctional CM-PDHs and four bifunctional prephenate-3-phosphoskimate 1-carboxyvinyltransferases (PDH-3-PSKs) were used for alignment. Monofunctional PDHs were as follows: *A. aeolicus* NP_214202, *Geobacter sulfurreducens* AAR35979, *Thermus thermophilus* YP_144065, *Campylobacter jejuni* YP_178149, *Neisseria meningitides* CAB85263, and *Deinococcus radiodurans* NP_294846. CM-PDHs were as follows: *E. coli* NP_289153, *Salmonella choleraesuis* YP_217658, *Erwinia carotovora* CAG76249, *Vibrio parahemeolyticus* NP_796926, *Blochmannia floridanus* NP_878481, *Pasteurella multocida* AAK02748, *Shewanella frigidimarina* ZP_00640059, *Mannheimia succiniciproducens*, AAU37709, and *Colwellia psychrerythraea* YP_270611. PDH-3-PSKs were as follows: *Acinetobacter calcoaceticus* CAG69018, *Pseudomonas syringae* NP_791573, *Pseudomonas fluorescens* YP_261402, *Pseudomonas aeruginosa* NP_251854, and *Pseudomonas putida* NP_743926.

RESULTS AND DISCUSSION

Limited Proteolysis to Determine Constructs Suitable for Crystallization—The overexpression of the FL *A. aeolicus* PDH in *E. coli* resulted in two protein products, a 36-kDa species corresponding to the intact protein and a 32-kDa degradation product (Fig. 1). The Ni-NTA purification profile, as judged by SDS-PAGE, revealed that the majority of the smaller sized protein flowed through the Ni-NTA column, whereas a higher proportion of the FL protein was bound to the column; SDS-PAGE analysis of the purified proteins indicated that roughly 80% of the total protein collected corresponds to the FL protein (Fig. 1). This result indicates that the low molecular weight species is a C-terminal fragment that lacks the N-terminal hexahistidine tag. Crystallization of

this protein mixture resulted in crystals that were sensitive to physical perturbations in the crystallization environment, such as vibration or changes in temperature. SDS-PAGE analysis of these protein crystals revealed that the smaller protein fragment is the major species contributing to crystal growth. In order to improve the quality of the protein crystal, we designed a number of expression constructs.

A limited tryptic digestion approach was applied to identify a protease-resistant fragment of PDH. Judging from the SDS-PAGE analysis, a stable fragment of ~32 kDa resulted from partial digestion (Fig. 1, *inset*). The ability of this fragment to resist the tryptic digestion suggested that its protease recognition motifs are not easily accessible, which, in turn, indicated that this fragment is tightly folded. In-gel tryptic digestion followed by mass spectrometry resulted in about 60% peptide coverage. Peptides identified include a peptide starting at residue 58 and the C-terminal peptide as well as other peptides between the former and the latter. Since peptides representing the first 58 residues were not identified by mass spectrometry, we proposed that the protease-susceptible region lies N-terminal to residue 58. Therefore, six expression constructs of the PDH protein, Δ19-PDH, Δ25-PDH, Δ28-PDH, Δ36-PDH, Δ52-PDH, and Δ55-PDH, were prepared and expressed. These constructs lack the first 19, 25, 28, 36, 52, and 55 residues, respectively.

Constructs Δ36-PDH, Δ52-PDH, and Δ55-PDH were unstable, whereas Δ19-PDH, Δ25-PDH, and Δ28-PDH produced stable and soluble proteins. The Δ19-PDH construct displays biophysical and kinetic properties similar to those of the FL PDH.[6] Crystallization of all soluble constructs was attempted, but only Δ19-PDH produced well ordered crystals. Crystals that diffracted to 1.9 Å resolution were obtained in an optimized crystallization solution containing 12% polyethylene glycol 4000, 100 mM sodium acetate at pH 3.2 and 200 mM lithium sulfate.

Structure Determination—Protein crystals of Δ19-PDH belong to space group $P2_1$ with unit cell dimensions of 42.7 × 178.9 × 75.2 Å. There are four PDH monomers in the asymmetric unit, and the Matthews coefficient is 2.05 $Å^3$/Da, which corresponds to an estimated solvent content of 40%. The final model of PDH consists of 1114 residues, four molecules of NAD^+, and 500 water molecules. In general, the electron density for the model is well defined, but the following residues have been excluded in the model due to weak electron densities: residues 20–29, 249–251, and 311 in Chain A, residues 20–30 and 311 in Chain B, residues 20–29 and 308–311 in Chain C, and residues 20–29 and 308–311 in Chain D. The final energy minimization refinement of PDH yields a protein model that has an *R* value of 22.08 (R_{free} of 26.30). The model displays excellent overall stereochemistry as judged by the Ramachandran plot, which shows that 99.8% of the residues are in the allowed regions. Data collection and refinement statistics are summarized in Table 2.

TABLE 2
Summary of x-ray data collection and refinement statistics
Numbers in parentheses refer to the highest resolution shell, 1.97–1.9 Å.

	Peak
X-ray data	
Space group	$P2_1$
Unit cell ($Å^3$)	42.7 × 178.9 × 75.2 $\beta = 99.2$
Resolution (Å)	30–1.9
Wavelength (Å)	0.9794
No. of selenium sites	28
No. of total observations	374,758
No. of unique observations	160,836
Redundancy	2.3
Intensity ($I/\sigma\langle I\rangle$)	11.9 (2.21)
Completeness (%)	91.9 (84.7)
R_{sym} [a]	0.072 (0.355)
Summary of refinement statistics	
R_{factor} [b]	22.08
R_{free}	26.30
No. of protein atoms	8812
No. of water molecules	500
No. of NAD^+ molecules	4
r.m.s.d.[c] bond lengths (Å)	0.006
r.m.s.d. bond angles (degrees)	1.17
r.m.s.d. dihedral (degrees)	20.7
r.m.s.d. improper (degrees)	0.84
Average *B* factor ($Å^2$)	29.30

[a] $R_{sym} = \Sigma|I - \langle I\rangle|/\Sigma I$, where *I* is the observed intensity, and $\langle I\rangle$ is the average intensity from multiple observations of symmetry-related reflections.
[b] $R_{factor} = \Sigma|F_o - F_c|/|F_o|$.
[c] r.m.s.d., root mean square deviation.

Overview of the Structure—The PDH monomer consists of two domains, an N-terminal α/β dinucleotide-binding domain (residues 31–200) and a C-terminal α-helical domain (residues 202–310) (Fig. 2). The N- and C-terminal domains associate though interactions involving regions of α4, α5, α8, α10, α11, β6, β7, β8, and the coil region between β6 and α6. This interdomain interface consists predominantly of charged and polar residues. Some notable residues at this cleft include Arg^{250} and Arg^{102}, which form ion pairs with Glu^{153} and Asp^{261}, respectively.

The N-terminal α/β domain is represented by a modified Rossmann fold. The core of this domain consists of a parallel, six-stranded β-sheet (β1–β6; β-strand order 3-2-1-4-5-6) that is sandwiched by two helices (α1 and α2) and a 3_{10} helix (α6) on one face of the sheet, and by three helices (α3–α5) on the other face (Fig. 2). This portion of the N-terminal domain is similar to other dinucleotide folds seen in NAD(P)-binding oxidoreductases, but it does contain a few deviations. For example, in addition to this conserved nucleotide-binding element, a β-α-β motif (β7-α7-β8) is appended to the central β-sheet. This motif lies adjacent to β6 of the core β-sheet and is twisted 60° out of plane with respect to the central β-sheet (Fig. 2*A*). Also, a long loop (residues 140–166) that is disrupted by a 3_{10} helix (α6) in the middle connects this β-α-β motif to the nucleotide-binding domain (Fig. 2). This connecting loop, found between β6 and β7, plays important functional roles in PDH. It adopts a "lasso" type conformation, which caps most of the PDH active site. Moreover, this loop is positioned adjacent to another loop (residues 240–247) formed by the second subunit of the dimer (Fig. 3*A*). Both loops participate in hydrogen bonding interactions with each other, and it is likely that these interactions could result in a gated mechanism allowing prephenate access to the active site. Residues from this functional loop also contribute to the active site architecture, since Glu^{153} and $Asp^{247'}$ form an ionic network with Arg^{250} (Fig. 3*A*), a conserved residue that has been shown to be important for prephenate binding (17).

The C-terminal domain adopts a novel, entirely helical architecture and is involved in subunit dimerization. This domain consist of five helices (α8, α10–α13) and one 3_{10} helix (α9) (Fig. 2). The helices are arranged in a highly twisted fashion, most of which are interrupted by tight turns consisting of just two residues. A long helical pair is formed by α12 and α13 and is positioned around a central helix, α8. α8 spans the entire length of the C-terminal domain and links it to the N-terminal domain.

Description of the Dimer—Although PDH crystallized as a tetramer in the asymmetric unit, only three pairs of interdimer interactions were identified. As such, the tetramer is represented as a dimer of dimers, with each existing as an independent unit. This observation is also consistent with gel filtration studies, which indicated that the protein is dimeric in solution (data not shown). Each dimer is formed by two tightly packed monomers that are interacting with one another via a tail-to-tail arrangement. This arrangement results in a dumbbell-shaped molecule consisting of a central helical axis that connects the two dinucleotide-binding domains (Fig. 3). This helical axis is formed by the C-terminal domains of the two monomers.

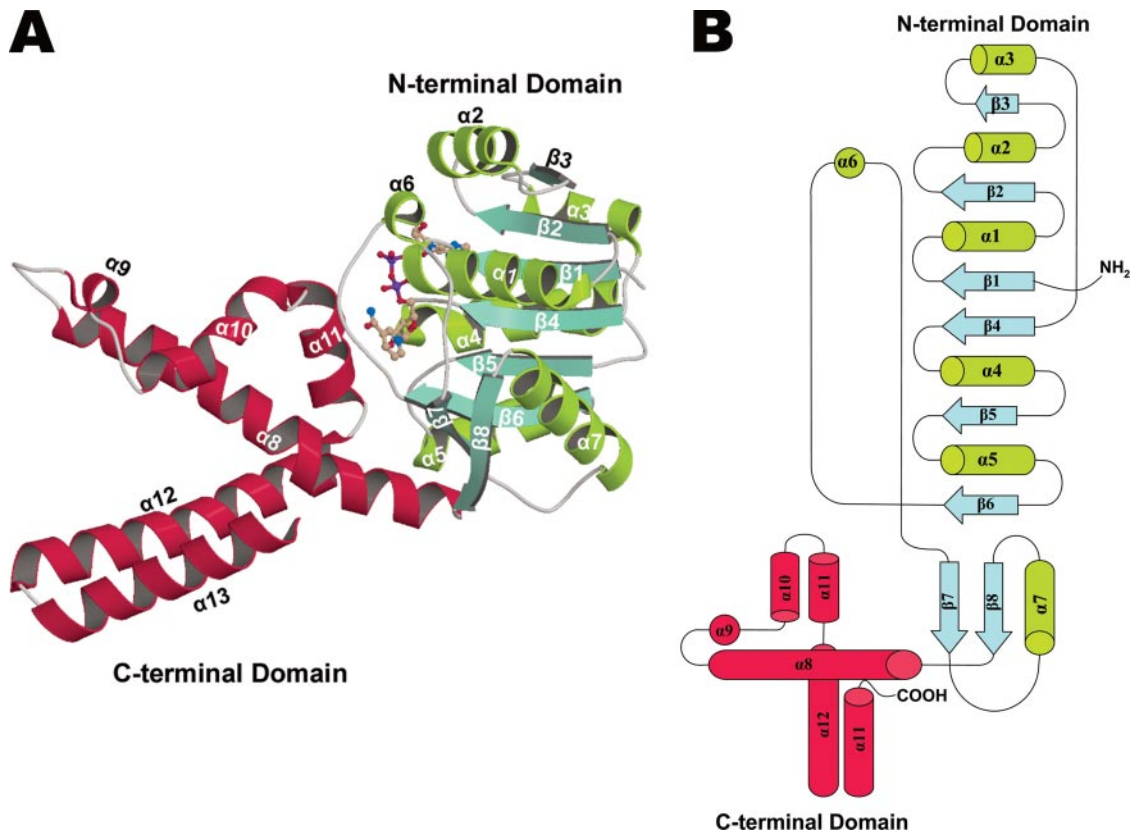

FIGURE 2. **Ribbon and topology diagrams of the PDH monomer.** *A*, the ribbon diagram of the monomer shows that the subunit consists of two domains, an N-terminal dinucleotide-binding domain (strands and helices are *colored cyan* and *green*, respectively) and a C-terminal domain composed entirely of helices (*red*). *B*, topology diagram of the PDH monomer shows the arrangement of secondary structures of the two domains. α-Helices are represented as *cylinders*, 3_{10} helices as *circles*, and β-strands as *arrows*. The *color scheme* is retained from *A*.

Dimerization Interface—In the PDH dimer, the monomers are closely associated through extensive, mainly hydrophobic interactions involving the helices of the C-terminal domains (Fig. 3). The resulting interactions produce a buried surface of 7452 Å^2. The C-terminal helices are arranged such that antiparallel helical pairs are formed between α8 and α8′, α10 and α10′, and α12 and α12′ (Fig. 3*C*), which results in reciprocal interactions. Moreover, these helical pairs also interact in a criss-cross manner between sets of pairs (Fig. 3, *B* and *C*). Consequently, the overall arrangement of the helices produces an intertwined and tightly packed helical bundle that is capped by α11 at one end and α11′ at the other. In addition, α13 and α13′ form the scaffold for this helical domain.

Since the dimer is formed by pair-wise and criss-cross interactions of the helices, the hydrophobic interactions at the interface are formed from the different helices. The helical pair consisting of α8 and α8′ is located at the core of the dimer interface and contributes significantly to dimer stability mainly through hydrophobic interactions. Helices α10 and α10′ provide few intersubunit contacts, but a noteworthy ionic interaction occurs between Arg^{250} and Asp$^{247′}$, residues that we propose modulate substrate access to the active site. Near the center of the α12-α12′ helical pair is a π-stacking interaction between Phe^{277} and Phe$^{277′}$. Also within this region is a large ionic network formed by Glu^{275}, Glu^{278}, and Lys^{285} from one subunit and Glu$^{275′}$, Glu$^{278′}$, and Lys$^{285′}$ from the other subunit. Since this PDH belongs to the hyperthermophile *A. aeolicus*, we expect that these interactions may contribute to the thermostability of the enzyme.

Structure of A. aeolicus PDH Represents a Novel Fold—DALI (33) analysis of the PDH monomer did not identify any structural homologs. The proteins identified with the queried monomer are a result of conservation at the N terminus. Analysis of the individual domains reveals that the N-terminal domain has homology to α/β dinucleotide folds, whereas the C-terminal domain does not have any significant relationship with known structures to date. Therefore, this first representative structure of a PDH enzyme from *A. aeolicus* represents a novel fold.

DALI identified numerous oxidoreducatses that have structural similarities to the N-terminal nucleotide-binding domain of PDH. The top five DALI hits are *Homo sapiens* L-3-hydroxyacyl-CoA dehydrogenase (34) (Protein Data Bank code 2hdh; Z score = 16.8), *E. coli* ketopantoate reductase (35) (Protein Data Bank code 1ks9; Z score = 15.4), *T. thermophilus* hydroxyisobutyrate dehydrogenase (36) (Protein Data Bank code 1j3v; Z score = 15.0), *Methanobacterium thermoautotrophicum* Mth1747 conserved hypothetical protein (Protein Data Bank code 1i36, Z score = 14.9), and *Streptococcus pyogenes* 1-pyrroline-5-carboxylate reductase (37) (Protein Data Bank code 2ahr; Z score = 14.3). Interestingly, these identified proteins belong to the 6-phosphogluconate dehydrogenase C-terminal domain-like superfamily as classified by the SCOP (structural classification of proteins) data base (38). This superfamily is characterized by an N-terminal Rossmann fold with a family-specific C-terminal extension whose common core is formed around two long antiparallel helices.

The N-terminal domain of PDH superposed well with the NAD(P)-binding domains of the above mentioned structural homologs. This analysis revealed that the β-α-β addition of the Rossmann fold is conserved among these proteins; however, some variations were detected. First, as seen in *H. sapiens* L-3-hydroxyacyl-CoA dehydrogenase, an additional helix is included in the region corresponding to α2 and β3 in PDH, and, in the case of *E. coli* ketopantoate reductase, β3 is lengthened

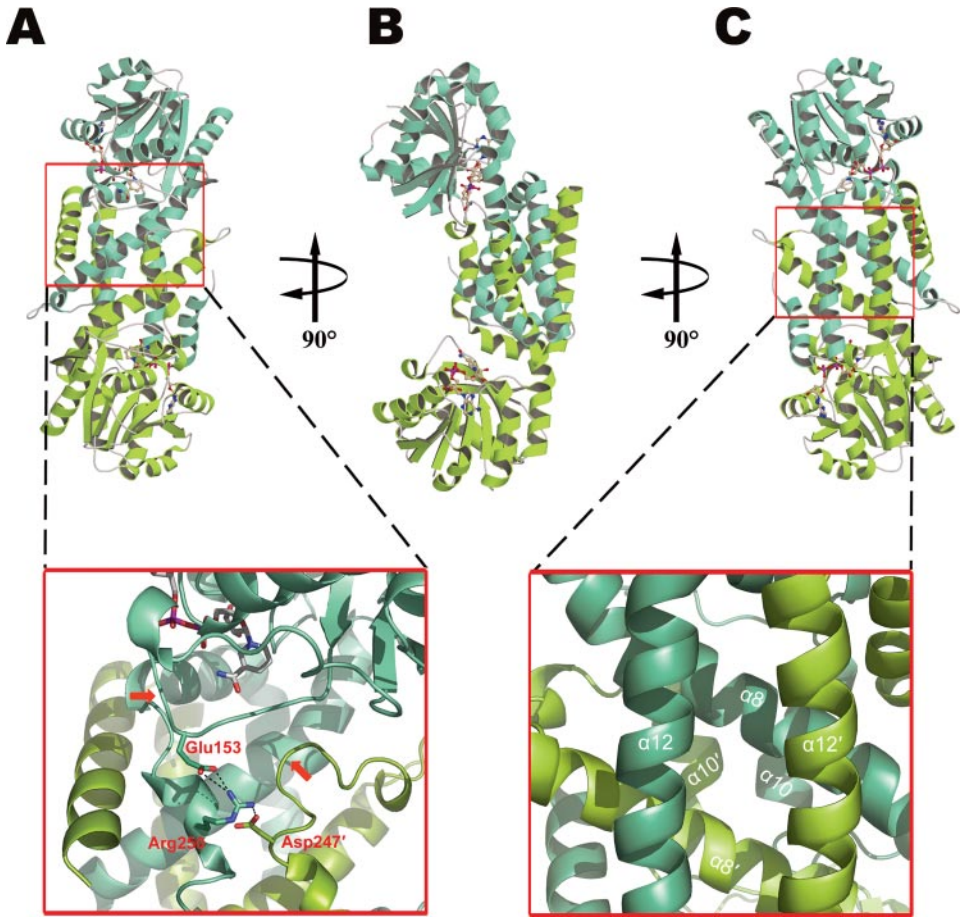

FIGURE 3. **Ribbon diagrams of the PDH homodimer showing important intersubunit interactions.** *B* is rotated 90° with respect to *A*, and *C* is rotated 90° with respect to *B*. One subunit is *colored cyan*, and the other is *green*. *A*, the active site is located mainly at the N-terminal domain of each monomer but is formed by contributions from both monomers. The enlargement (*box*) shows the position of the nicotinamide ring with respect to the pocket formed at the dimer interface. The pocket is gated by two main loops (*arrows*), which are bridged together by a Glu^{153}-Arg^{250}-$Asp^{247'}$ ionic network. This gated structure could mediate the entry of prephenate into the active site. *B*, the arrangement of the subunits results in a dumbbell-shaped molecule with both C-terminal domains forming the axis of the dumbbell and each N-terminal domain forming a bell of the dumbbell. *C*, the arrangement of the C-terminal helices results in a criss-cross structure consisting of three sets of antiparallel helical pairs. The enlarged view (*box*) shows that the α12-α12′ helical pair crosses the α8-α8′ helical pair which, in turn, crosses the α10-α10′ pair.

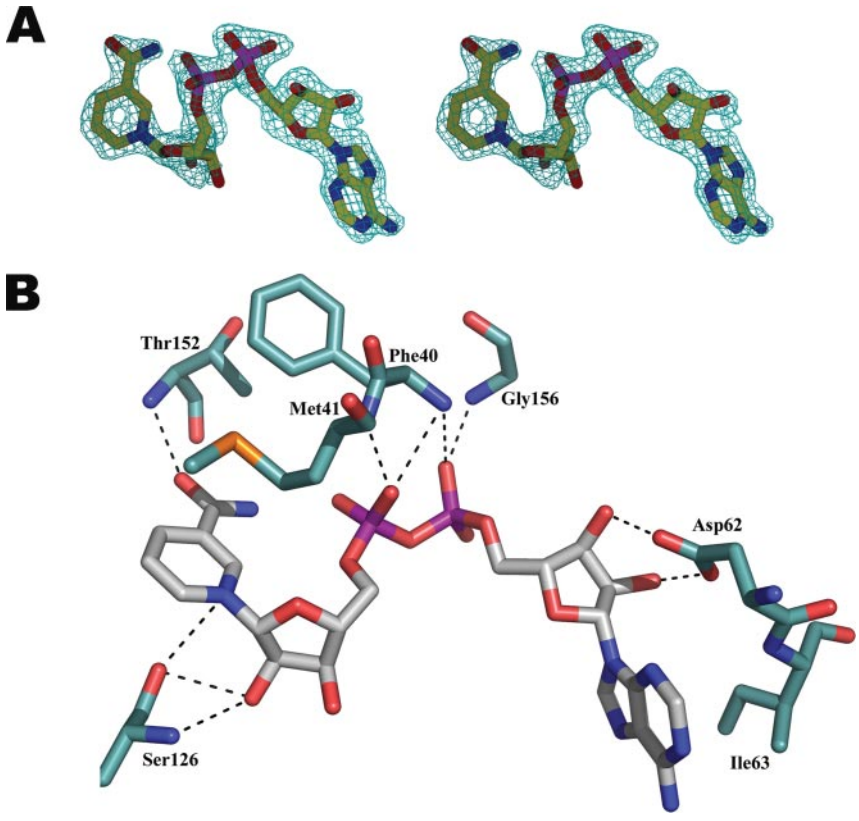

FIGURE 4. **Electron density map and key PDH-NAD^+ interactions.** *A*, a stereo view of the electron density of a representative NAD^+ molecule. The final NAD^+ molecule is shown in the original density obtained after phasing and density modification by RESOLVE. The map is contoured at 1.0 σ. *B*, interactions with NAD^+ are typical of those seen in other NAD^+-binding proteins. The backbone amides of Phe^{40} and Met^{41} from the G*X*G*XX*G motif form hydrogen bonds to the oxygen atoms of the pyrophosphate moiety, and Asp^{62} interacts with the diol groups of the adenylyl moiety. In addition, Ser^{126} plays a major role in orientating the nicotinamide moiety by hydrogen-bonding to a ribose hydroxyl and to the N-1 atom of the nicotinamide moiety.

along with β4. Finally, the coil regions between β6 and β7 are extended in *A. aeolicus* PDH to form a large lasso-like structure.

DALI analysis of the C-terminal domain identified a number of structures but with low Z scores (Z scores from 3.7 to 2.0). The nonstructural protein (NS1 protein) of the influenza A virus (39) (Protein Data Bank code 1ail; Z score = 3.7) is the closest structural homologue to this domain of PDH. This protein contains an RNA-binding domain that is entirely helical. However, comparative structural analysis failed to show a significant match in topologies between the C-terminal domain of PDH and the NS1 protein. Thus, no structural insight could be inferred from this analysis.

Binding Environment of the NAD^+ Cofactor—PDH crystals were grown in the presence of 1 mM NAD^+. Clear electron density was consistently observed for this cofactor in the nucleotide-binding pocket after two rounds of refinement (Fig. 4*A*); therefore, the NAD^+ molecule was subsequently built in. The nicotinamide moiety adopts an *anti*-conformation, since the ring is rotated outward from the *N*-glycosidic bond.

The pyrophosphate moiety of NAD^+ interacts with a glycine-rich loop between β1 and α1. The residues in this loop comprise the *GXGXXG* fingerprint motif that is characteristic of NAD(P)-dependent oxidoreductases. In PDH, these residues are Gly^{37}, Val^{38}, Gly^{39}, Phe^{40}, Met^{41}, and Gly^{42} (Fig. 4*B*). The most prominent interactions involve residues Phe^{40} and Met^{41}, whose main chain amides hydrogen bond to the phosphate oxygen atoms of NAD^+. Specifically, the main chain amide of Met^{41} hydrogen bonds to the O-1 atom of the adenylyl moiety, whereas the amide of Phe^{40} hydrogen bonds to both O-1 atoms of the pyrophosphate moiety. In addition to these interactions, Gly^{156} hydrogen bonds to the O-1 atom of the adenylyl moiety via its main chain amide.

The diol group of the adenylyl ribose and the A face of adenine are bound in part to the enzyme by Tyr^{61}, Asp^{62}, and Ile^{63}. These residues are located in the loop connecting β2 to α2. Asp^{62} hydrogen-bonds to both hydroxyl groups of the adenylyl ribose (Fig. 4*B*); this conserved aspartate specifies selectivity for NAD^+ binding (40, 41). Furthermore, the carboxylate side chain of this residue hydrogen-bonds to the main chain nitrogen of Val^{38}. Ile^{63} stacks with the A face of adenine and interacts hydrophobically with the delocalized π-system of the adenylyl ring (Fig. 4*B*). Tyr^{61}, although not directly involved in interactions with NAD^+, forms a hydrogen bond with Gly^{37} from the glycine-rich phosphate-binding motif via main chain interactions. In addition to the above mentioned interactions, a conserved water molecule bridges the N-6 atom of the adenylyl ring with Glu^{106} through hydrogen-bonding interactions.

The nicotinamide moiety of NAD^+ is the functional portion of the cofactor, since hydride transfer occurs at the C-4 position of this ring. Therefore, the orientation of the nicotinamide group is dependent on the substrate and is crucial for catalysis. A conserved serine, Ser^{126}, appears to be particularly important for the proper positioning of this ring (Fig. 4*B*). The main chain amide of Ser^{126} hydrogen bonds to the C-2 hydroxyl of the nicotinamide ribose. Furthermore, the side chain moiety of this serine also hydrogen-bonds with the above mentioned ribose hydroxyl and with the N-1 atom of the nicotinamide ring. Another important residue is Thr^{152}, which forms a hydrogen bond between its main chain amide and the O-7 atom of the nicotinamide ring (Fig. 4*B*). This residue, however, is not conserved, but this could be a consequence of low selection pressure, since this hydrogen bond involves the main chain atom.

Identification of the PDH Active Site—The identification of the putative PDH active site was accomplished by locating a cavity at the domain interface that is adjacent to the nucleotide-binding site. This analysis was facilitated by the determination of the enzyme structure in complex with NAD^+. The nicotinamide ring of NAD^+ was also found in this

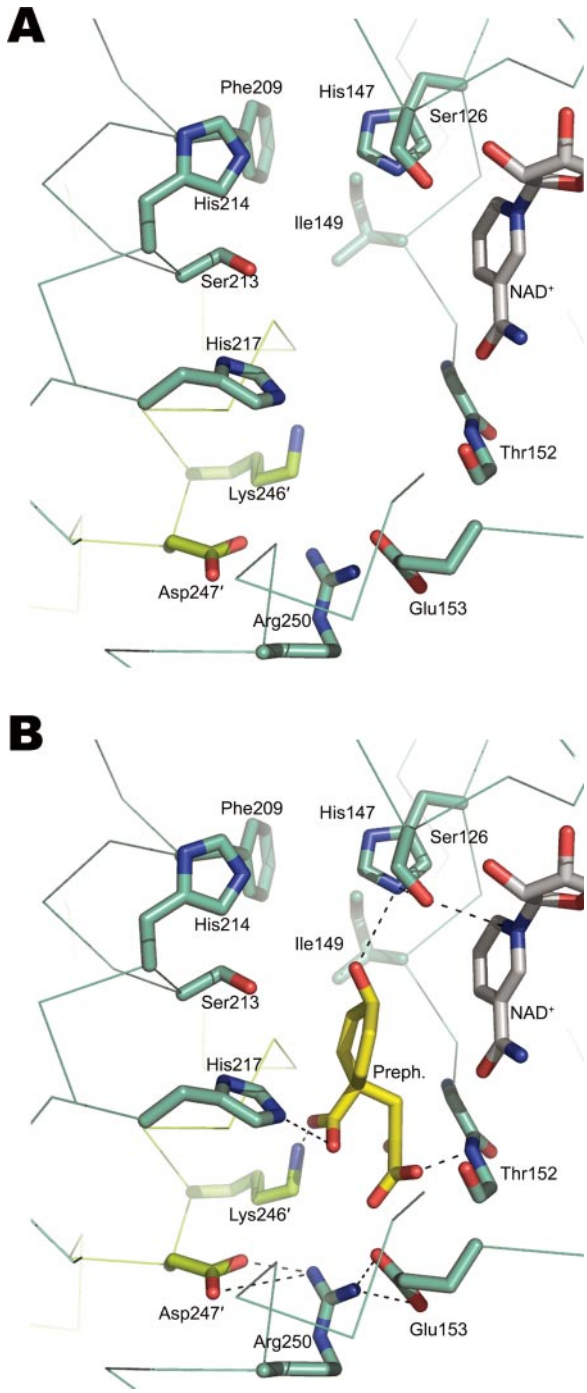

FIGURE 5. **The putative *A. aeolicus* active site.** *A*, a number of residues identified in the prephenate binding pocket include the catalytic base, His^{147}, and the conserved binding group, Arg^{250}, which are all juxtaposed to the NAD^+ nicotinamide ring. *B*, prephenate modeled into the active site shows the proposed interactions between some of the active site residues and substrate. The C-4 OH is proximal to His^{147}, and the nicotinamide C-2 OH and N-1 interact with Ser^{126}. The C-1 carboxyl and pyruvyl groups are within hydrogen bonding distance to Arg^{250}, His^{217}, and $Lys^{246'}$, where Arg^{250} participates in ionic interactions with $Asp^{247'}$ and Glu^{153}.

putative active site (Fig. 5*A*). Furthermore, we confirmed our finding by identifying previously implicated active site residues in this cavity.

The putative active site is located at the intersubunit interface; however, a large portion of the binding pocket is contained within one subunit, specifically at the interdomain cleft. From one subunit, regions of β6, α8, and α10 and the coil regions between β5 and α5 and between β6 and α6 comprise the majority of the active site pocket, whereas, in the

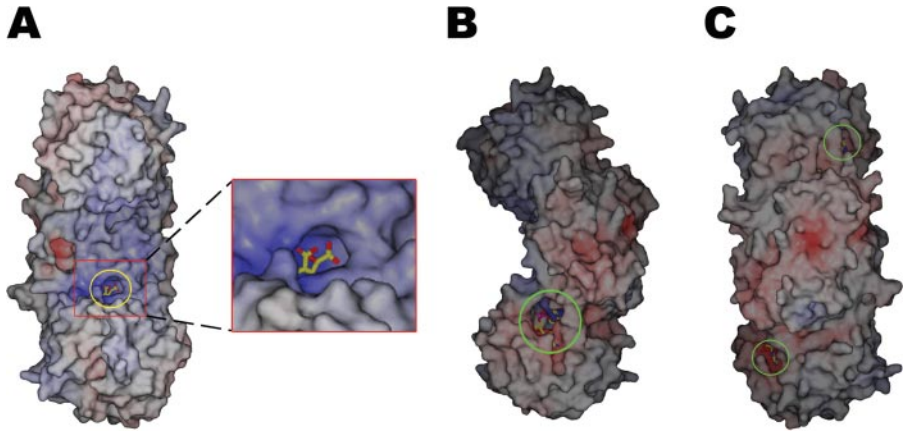

FIGURE 6. **Surface potential map of the PDH dimer.** *A–C* are oriented according to Fig. 2, *A–C*, respectively. *A*, a view showing a large region of basic residues, which comprise the prephenate binding pocket. An enlarged view of this region (*box*) shows prephenate modeled into the binding pocket. *B* and *C*, NAD^+ resides in a large cleft at the domain interface. The *yellow* and *green circles* indicate prephenate and NAD^+, respectively.

other subunit, regions of the turn preceding α10′ and α10′ itself complete the pocket. Analysis of this pocket revealed a highly polar active site. Briefly, Ser^{126}, His^{147}, Phe^{209}, and His^{214} are found at the base of the pocket, whereas Gly^{151}, Glu^{153}, Ser^{213}, His^{217}, $Gly^{242'}$, $Gly^{243'}$, $Gly^{244'}$, $Lys^{246'}$, Arg^{250}, and Trp^{259} line the walls of the active site (Fig. 5*A*).

Prephenate Interactions—To gain further insight into the interactions between prephenate and PDH, a prephenate molecule was modeled into the putative active site region (Fig. 5*B*) using the properties of known active site residues and the C-4 atom of the nicotinamide ring as guides. In particular, the conserved His^{147} and Arg^{250} residues were used as reference points to orient the prephenate molecule, since the equivalent histidine (His^{197}) and arginine (Arg^{294}) residues in the *E. coli* CM-PDH have been implicated as the catalytic base involved in hydride transfer and as the key group that binds prephenate via the ring carboxylate, respectively. Our placement of prephenate in the active site is further corroborated by the surface potential of PDH, which shows that the modeled prephenate molecule resides in a highly basic cleft that is proximal to NAD^+ (Fig. 6).

The prephenate molecule can be dissected into two functional domains, one for catalysis and the other for binding PDH. The C-4 of prephenate is considered the reactive center, since the hydride at this position is transferred to NAD^+ during the enzymatic reaction (42, 43). Thus, prephenate was modeled into the putative active site so that its C-4 is 2.5 Å away from the C-4 atom of the nicotinamide ring.

Kinetic analysis of the *E. coli* CM-PDH indicated that the C-4 hydroxyl of prephenate becomes polarized by a conserved catalytic base, which facilitates hydride transfer to NAD^+ (18). In the crystal structure, the prephenate C-4 hydroxyl points toward His^{147} and is within potential hydrogen bonding distance to this residue (Fig. 5*B*). In addition, the conserved Ser^{126} may indirectly affect catalysis, since it forms a hydrogen bond with His^{147} and with the N-1 atom of the nicotinamide ring (Fig. 5*B*).

At the C-1 position of prephenate, the ring carboxylate and the pyruvyl moiety are both found in a highly polar environment (Figs. 5*B* and 6*C*). In this region of the active site, we identified Arg^{250} and Glu^{153} from one subunit and $Lys^{246'}$ and $Asp^{247'}$ from the other subunit (Fig. 5*B*). Arg^{250} is poorly ordered, as judged by the quality of its electron density. This is consistent with existing kinetic data, which implicated this conserved arginine as a key binding group that interacts with prephenate through the ring carboxylate (17); the absence of a bound ligand, substrate, or substrate analogue can account for the disorder of this arginine residue. Thus, in agreement with the proposed interaction, the current conformation of Arg^{250} places its side chain in the vicinity of both the ring carboxylate and the pyruvyl side chain of prephenate.

Arg^{250} is located in the middle of helix α10 and also participates in a pair of ionic interactions with Glu^{153} and $Asp^{247'}$, both of which are located on the loop regions that cap the active site (Figs. 3*A* and 5*B*). We envision that these ionic interactions modulate the passage of substrate into the active site. A complete understanding of this gated mechanism will have to await structures from cocrystallization studies combined with the results from future mutagenesis studies.

$Lys^{246'}$ is also within interacting distance with the ring carboxylate and pyruvyl side chain. In the current conformation, it interacts with the ring carboxylate of prephenate (Fig. 5*B*). Interestingly, a series of semi-conserved glycines ($Gly^{242'}$, $Gly^{243'}$, $Gly^{244'}$) preceding $Lys^{246'}$ appears to be critical for positioning $Lys^{246'}$ into the active site for this interaction with prephenate. Although this glycine-rich region is not conserved in all sequences analyzed, other sequences contain a proline at the $Gly^{243'}$ position (Fig. 7).

Spatial Relationship of the PDH Domain—To examine the spatial relationship of the PDH domain within bifunctional PDHs, a multiple-sequence alignment of monofunctional PDHs with the PDH domains of both CM-PDHs and PDH-3-PSKs was conducted. The alignment identified a number of conserved residues (Fig. 7), including the conserved G*X*G*XX*G motif, which is characteristic of NAD(P)-binding proteins, and a conserved aspartate or arginine, which confers nucleotide, NAD^+ or $NADP^+$, specificity (41). Other conserved residues include His^{147}, Ser^{126}, Lys^{246}, and Arg^{250}, which are positioned in the active site. These residues are directly interacting with either the modeled prephenate or the nicotinamide ring of NAD^+. The positions of these residues in the active site and their putative interactions with prephenate were discussed earlier.

Monofunctional PDHs and the PDH domains of PDH-3-PSKs aligned without sizeable indels; however, the alignment of the monofunctional PDHs with the PDH domains of CM-PDHs included three large indels, Indel 1, Indel 2, and Indel 3 (Fig. 7). Indel 1 suggests that the PDH domain of CM-PDH lacks β3 and that α2 and α3 are shortened. All of these secondary structures are located at a terminal region of the nucleotide-binding domain (Fig. 2). Indel 2 indicates that β7 is missing; this β-strand is adjacent to β6 and is a part of the appended β-α-β motif (Fig. 2). The catalytic histidine, His^{147}, is located on β6, which forms the base of the active site pocket; therefore, we speculate that β7 provides a supporting role for β6 and may help to orient His^{147} into a catalytically competent position. At Indel 3, a series of glycines (Gly^{242}, Gly^{243}, Gly^{244}), which form part of the active site wall, have been substituted with a proline residue in all PDH domains of CM-PDHs analyzed. The role of this substitution will be investigated by future mutagenesis studies.

The above analyses suggest that the functional domains of CM-PDHs are structurally interdependent, whereas the functional domains of PDH-3-

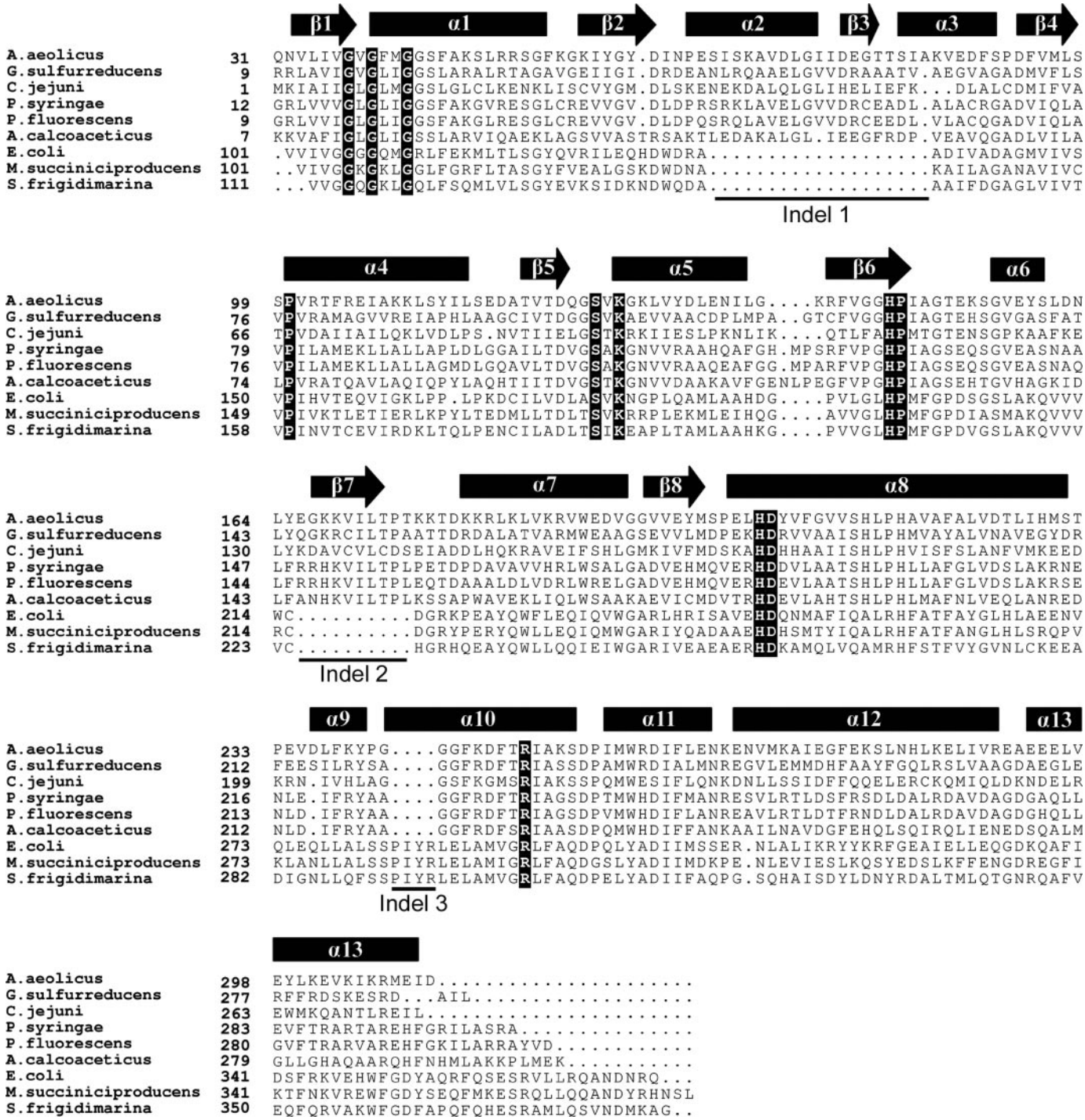

FIGURE 7. **Representative multiple sequence alignment of monofunctional PDHs and the PDH domains of CM-PDHs and PDH-3-PSKs.** Shown here are three sequences for each category of PDH: monofunctional PDHs (*A. aeolicus*, *G. sulfurreducens*, and *C. jejuni*), CM-PDHs (*E. coli*, *S. frigidimarina*, and *M. succiniciproducens*), and PDH-3-PSK (*A. calcoaceticus*, *P. syringae*, and *P. fluorescens*). Only strictly conserved residues are *highlighted* in *black*. The catalytic histidine and substrate-binding arginine are conserved in all sequences analyzed. In addition, all sequences contain the G*X*G*XX*G motif characteristic of NAD(P)-binding folds. The alignment also shows that monofunctional PDHs and the PDH domains of PDH-3-PSKs aligned without sizeable indels, whereas the monofunctional PDHs and the PDH domains of CM-PDHs aligned with three large indels, labeled *Indel 1*, *Indel 2*, and *Indel 3*.

PSKs are independent. Specifically, the CM domain of CM-PDH may be contributing structural elements to the PDH domain. This is consistent with biochemical and mutagenesis data of several residues in the PDH domain of *E. coli* CM-PDH that affected the k_{cat} and K_m of both CM and PDH (17, 18). These include the H189N mutant, which dramatically reduced k_{cat} by more than 1000-fold for both CM and PDH activities (18). In addition, the K178R, H131A, H239N, H245N, and H347N mutants affected both the turnover rate and substrate binding of the CM and PDH domains to differing degrees (17, 18). Attempts to separate the CM and PDH domains of the bifunctional *E. coli* enzyme by molecular means also indicated that neither could be expressed in a fully functional form as discrete, contiguous domains (44). Moreover, attempts to prepare a functional PDH domain from *Erwinia herbicola* CM-PDH indicated that only the first 37 residues of CM domain could be removed while retaining PDH activity (45). The interdomain dependence of CM-PDH may reflect the requirement for substrate channeling from the CM site to the PDH site for tyrosine

biosynthesis. This is consistent with the work of Heyde (31), which indicated that radiolabeled prephenate produced at the CM site is channeled to the PDH active site. In contrast to CM-PDH, our analyses suggest that the functional domains of PDH-3-PSK are structurally independent. PDH-3-PSK could be a result of gene fusion, and we would thus expect that they can be separated. Indeed, a complementation study with the PDH domain of PDH-3-PSK from *P. stutzeri* supports our hypothesis (30). Further validation of this hypothesis will be accomplished by mutagenesis and limited proteolysis studies to separate the PDH domain from the 3-PSK domain.

Correlation of Existing Kinetic Data—The current placement of prephenate in the active site of PDH is corroborated with existing mutagenesis and kinetic data. Kinetic data from *E. coli* CM-PDH implicates the conserved His^{147} as the key catalytic group that polarizes the C-4 hydroxyl of prephenate to facilitate hydride transfer (18). This is consistent with our findings, since His^{147} is near the C-4 position of the nicotinamide ring of NAD^+ and is within hydrogen bonding distance to the C-4 hydroxyl of the modeled prephenate (Fig. 5*B*). We also identified a conserved serine, Ser^{126}, which hydrogen-bonds to His^{147} and to the C-2 hydroxyl and N-1 atom of the nicotinamide ring (Figs. 4*B* and 5*B*). The mechanistic role of this residue has not been evaluated before; however, these interactions suggest that Ser^{126} could play a major role in orienting both His^{147} and the nicotinamide moiety of NAD^+ in their catalytically efficient conformations.

The conserved Arg^{250} has been implicated as a key binding group, which interacts via the ring carboxylate of prephenate (17). This is consistent with our findings, which place Arg^{250} in the vicinity of both the ring carboxylate and the pyruvyl moiety of prephenate (Fig. 5*B*). Determination of the direct role of this residue in prephenate binding awaits cocrystallization studies with either prephenate or substrate analogues. In addition, Arg^{250} may be involved in modulating the access of prephenate to the active site, since conformational changes upon substrate binding could change the positioning of Arg^{250} and its interactions with Glu^{153} and $Asp^{247'}$ (Figs. 3*A* and 5*B*).

The conserved Lys^{128} was also investigated by kinetic analysis. In the *E. coli* CM-PDH, the equivalent lysine residue, Lys^{178}, was mutated to an arginine, which resulted in an unstable protein with a greatly reduced capacity for binding prephenate and NAD^+ (17). From structural analysis, we have now determined the role of this conserved lysine. Lys^{128} is found at the N-terminal end of α5 and hydrogen-bonds with Asp^{123}, which is located in β5. In addition, Lys^{128} also hydrogen-bonds with the main chain carbonyl groups of Gly^{125} and Val^{127}, both of which are located in the coil region linking α5 to β5. Collectively, these interactions result in the protrusion of the aforementioned coil into the active site, and, most notably, this allows Ser^{126} to point into the active site pocket. The *E. coli* K178R mutation probably disrupted most of these interactions as well as affected the conformation of active site residues that had a pronounced effect on substrate binding.

This first representative structure from the PDH family of enzymes has given us the opportunity to interpret existing kinetic data. In addition, we have identified new active site residues and have proposed a novel mechanism for modulating the access of prephenate into the active site. Consequently, the results presented provide a framework for future investigations of PDH. Moreover, our understanding of the PDH structure-function relationship has been greatly advanced. This will provide a basis for investigating the mechanism of substrate discrimination between the different classes of TyrA enzymes as well as facilitate the rational design of drugs targeting tyrosine biosynthesis.

REFERENCES

1. Meganathan, R. (2001) *FEMS Microbiol. Lett.* **203,** 131–139
2. Rescigno, A., Rinaldi, A. C., and Sanjust, E. (1998) *Biochem. Pharmacol.* **56,** 1089–1096
3. Moller, B. L., and Conn, E. E. (1979) *J. Biol. Chem.* **254,** 8575–8583
4. Frick, S., and Kutchan, T. M. (1999) *Plant J.* **17,** 329–339
5. Memelink, J. (2004) *Nat. Biotechnol.* **22,** 1526–1527
6. Kaneko, M., Hwang, E. I., Ohnishi, Y., and Horinouchi, S. (2003) *J. Ind. Microbiol. Biotechnol.* **30,** 456–461
7. Mobley, E. M., Kunkel, B. N., and Keith, B. (1999) *Gene* (*Amst.*) **240,** 115–123
8. Taylor, L. P., and Grotewold, E. (2005) *Curr. Opin. Plant Biol.* **8,** 317–323
9. Buer, C. S., and Muday, G. K. (2004) *Plant Cell* **16,** 1191–1205
10. Brown, D. E., Rashotte, A. M., Murphy, A. S., Normanly, J., Tague, B. W., Peer, W. A., Taiz, L., and Muday, G. K. (2001) *Plant Physiol.* **126,** 524–535
11. Guyon, V., Tang, W. H., Monti, M. M., Raiola, A., Lorenzo, G. D., McCormick, S., and Taylor, L. P. (2004) *Plant J.* **39,** 643–654
12. Taylor, L. P., and Hepler, P. K. (1997) *Annu. Rev. Plant Physiol. Plant Mol. Biol.* **48,** 461–491
13. Kobayashi, H., Naciri-Graven, Y., Broughton, W. J., and Perret, X. (2004) *Mol. Microbiol.* **51,** 335–347
14. Bonner, C. A., Jensen, R. A., Gander, J. E., and Keyhani, N. O. (2004) *Biochem. J.* **382,** 279–291
15. Cotton, R. G., and Gibson, F. (1965) *Biochim. Biophys. Acta* **100,** 76–88
16. Song, J., Bonner, C. A., Wolinsky, M., and Jensen, R. A. (2005) *BMC Biol.* **3,** 1–30
17. Christendat, D., and Turnbull, J. L. (1999) *Biochemistry* **38,** 4782–4793
18. Christendat, D., Saridakis, V. C., and Turnbull, J. L. (1998) *Biochemistry* **37,** 15703–15712
19. Dill, G. M. (2005) *Pest Manag. Sci.* **61,** 219–224
20. Roberts, C. W., Roberts, F., Lyons, R. E., Kirisits, M. J., Mui, E. J., Finnerty, J., Johnson, J. J., Ferguson, D. J., Coggins, J. R., Krell, T., Coombs, G. H., Milhous, W. K., Kyle, D. E., Tzipori, S., Barnwell, J., Dame, J. B., Carlton, J., and McLeod, R. (2002) *J. Infect. Dis.* **185,** Suppl. 1, 25–36
21. Christendat, D., Saridakis, V., Dharamsi, A., Bochkarev, A., Pai, E. F., Arrowsmith, C. H., and Edwards, A. M. (2000) *J. Biol. Chem.* **275,** 24608–24612
22. Sambrook, J. F. E., and Maniatis, T. (1989) *Molecular Cloning: A Laboratory Manual*, Cold Spring Harbor Laboratory Press, Cold Spring Harbor, NY
23. Otwinowski, Z., and Minor, W. (1997) *Methods Enzymol.* **276,** 307–326
24. Terwilliger, T. C., and Berendzen, J. (1999) *Acta Crystallogr. Sect. D Biol. Crystallogr.* **55,** 849–861
25. Terwilliger, T. C. (2000) *Acta Crystallogr. Sect. D Biol. Crystallogr.* **56**, 965–972
26. Perrakis, A., Morris, R., and Lamzin, V. S. (1999) *Nat. Struct. Biol.* **6,** 458–463
27. Jones, T. A., Zou, J. Y., Cowan, S. W., and Kjeldgaard, M. (1991) *Acta Crystallogr. Sect. A* **47**, 110–119
28. Brunger, A. T., Adams, P. D., Clore, G. M., DeLano, W. L., Gros, P., Grosse-Kunstleve, R. W., Jiang, J. S., Kuszewski, J., Nilges, M., Pannu, N. S., Read, R. J., Rice, L. M., Simonson, T., and Warren, G. L. (1998) *Acta Crystallogr. Sect. D Biol. Crystallogr.* **54**, 905–921
29. Kraulis, P. J. (1991) *J. Appl. Crystallogr.* **24,** 946–950
30. Xie, G., Bonner, C. A., and Jensen, R. A. (2000) *Comp. Biochem. Physiol. C Toxicol. Pharmacol.* **125,** 65–83
31. Heyde, E. (1979) *Biochemistry* **18,** 2766–2775
32. Notredame, C., Higgins, D. G., and Heringa, J. (2000) *J. Mol. Biol.* **302,** 205–217
33. Holm, L., and Sander, C. (1995) *Trends Biochem. Sci.* **20,** 478–480
34. Barycki, J. J., O'Brien, L. K., Bratt, J. M., Zhang, R., Sanishvili, R., Strauss, A. W., and Banaszak, L. J. (1999) *Biochemistry* **38,** 5786–5798
35. Matak-Vinkovic, D., Vinkovic, M., Saldanha, S. A., Ashurst, J. L., von Delft, F., Inoue, T., Miguel, R. N., Smith, A. G., Blundell, T. L., and Abell, C. (2001) *Biochemistry* **40,** 14493–14500
36. Lokanath, N. K., Ohshima, N., Takio, K., Shiromizu, I., Kuroishi, C., Okazaki, N., Kuramitsu, S., Yokoyama, S., Miyano, M., and Kunishima, N. (2005) *J. Mol. Biol.* **352,** 905–917
37. Nocek, B., Chang, C., Li, H., Lezondra, L., Holzle, D., Collart, F., and Joachimiak, A. (2005) *J. Mol. Biol.*
38. Murzin, A. G., Brenner, S. E., Hubbard, T., and Chothia, C. (1995) *J. Mol. Biol.* **247,** 536–540
39. Liu, J., Lynch, P. A., Chien, C. Y., Montelione, G. T., Krug, R. M., and Berman, H. M. (1997) *Nat. Struct. Biol.* **4,** 896–899
40. Carugo, O., and Argos, P. (1997) *Proteins* **28,** 10–28
41. Lesk, A. M. (1995) *Curr. Opin. Struct. Biol.* **5,** 775–783
42. Hermes, J. D., Tipton, P. A., Fisher, M. A., O'Leary, M. H., Morrison, J. F., and Cleland, W. W. (1984) *Biochemistry* **23,** 6263–6275
43. Turnbull, J., Cleland, W. W., and Morrison, J. F. (1991) *Biochemistry* **30,** 7777–7782
44. Chen, S., Vincent, S., Wilson, D. B., and Ganem, B. (2003) *Eur. J. Biochem.* **270,** 757–763
45. Xia, T., Zhao, G., Fischer, R. S., and Jensen, R. A. (1992) *J. Gen. Microbiol.* **138,** 1309–1316